

THESIS / THÈSE

DOCTOR OF SCIENCES

Selective growth of CdTe by molecular beam epitaxy on CdTe(211)B microseeds and Si(100) nanoseeds patterned on SiO₂

Seldrum, Thomas

Award date:
2009

Awarding institution:
University of Namur

[Link to publication](#)

General rights

Copyright and moral rights for the publications made accessible in the public portal are retained by the authors and/or other copyright owners and it is a condition of accessing publications that users recognise and abide by the legal requirements associated with these rights.

- Users may download and print one copy of any publication from the public portal for the purpose of private study or research.
- You may not further distribute the material or use it for any profit-making activity or commercial gain
- You may freely distribute the URL identifying the publication in the public portal ?

Take down policy

If you believe that this document breaches copyright please contact us providing details, and we will remove access to the work immediately and investigate your claim.

Chapter III. Experimental Techniques

III.1. Ultra high vacuum environment

Analyzing, modifying and monitoring the properties of the surface require an environment with a base pressure below 10^{-10} mbar. This low pressure is called ultra high vacuum (UHV) condition. Three major advantages arise from working in UHV conditions:

- Because of the low pressure, the time required to cover the surface with one monolayer (ML) of contaminants is long compared to the time needed to analyze or modify the surface. Contamination arises from the adsorption of molecules on the surface. These contaminants come from desorption of water (this can be avoided by baking the chamber at 120°C for several days) and other adsorbed gases from the walls of the chamber and from residual gases of evaporation sources. These contaminants are responsible for the limitation of the pressure P measured in the chamber. To calculate the time τ needed to adsorb 1 ML (expressed in number of adsorption sites per square meter), the flux of molecules arriving on the surface has to be determined. If the pressure P is composed of molecules of mass m and if the chamber temperature is T , the flux arriving per second on a square meter is:

$$\Gamma_{\text{sample}} \left(m^{-2} s^{-1} \right) = \frac{P}{\sqrt{2mkT}} \quad (3.1)$$

Assuming that each molecule arriving on the surface is adsorbed (i.e. considering a sticking coefficient of 1), the time required to cover the surface with 1 ML of contaminant is:

$$\tau(s) = \frac{1ML}{\Gamma_{\text{sample}}} \quad (3.2)$$

- The second advantage of working under UHV conditions is that filaments (in Ta, W or LaB₆) can be heated to high temperature without burning (because of evaporation of the metal oxidized in presence of oxygen). The filaments are required for several purposes, among which:
 - Emitting electrons which can then be focused on the sample to perform electron based analysis techniques (see RHEED, LEED or AES in the following sections);
 - Using the emitted radiation to heat a sample placed close to the filament (in the following text, this heating mode is called radiative heating).

- Under UHV conditions, a particle travels a distance called mean free path (λ) before colliding with another particle. This distance depends on the pressure and the temperature in the chamber and the diameter d of the molecule:

$$\lambda = \frac{kT}{\sqrt{2P\pi}d^2} \quad (3.3)$$

III.2. Electron diffraction techniques

III.2.A. History

Using experimental and theoretical discoveries about the wave – particle duality applied to electrons, Davisson and Germer presented, in 1927 [19], the first diffraction pattern obtained by low energy electron diffraction technique (LEED). Indeed, according to the wave – particle duality, a wavelength λ can be associated to an electron characterized by an energy $E=h\nu$ and a momentum p :

$$p = \frac{h\nu}{c} \rightarrow \lambda = \frac{h}{p} = \sqrt{\frac{h^2}{2mE}} \quad (3.4)$$

where h is the Plank's constant.

In the equation (3.4), if the wavelength λ is expressed in nm and the energy E is in electron volts (eV), the wavelength associated to an electron is:

$$\lambda = \frac{1.23}{\sqrt{E}} \quad (3.5)$$

If the electron beam interacts with a surface whose crystalline lattice parameter is in the same order of magnitude as the wavelength of the electrons (this can be done by tuning the energy of the electron), diffraction can be observed. Depending on geometric considerations, the phase difference between the wave vectors of the diffracted beams produces a constructive or a destructive interference. In conclusion, diffraction techniques allow one to probe the reciprocal space of a crystal and are a suitable tool for the crystalline quality study.

For all electron based diffraction techniques, the key point is that the electrons are charged particles, and the consequence is a strong interaction between the electrons and the matter. As a result their mean free path is reduced to the nanometer scale and the incident beam interacts only with the extreme surface of the analyzed sample. Among the electron diffraction based analysis techniques developed, two of them are used to check the cristallinity of the surface:

low energy electron diffraction (LEED) and reflection high energy electron diffraction (RHEED). The UHV environment ensures that the mean free path of the electrons is far larger than the dimensions of the chamber, so it is easy to focus the electron beam on the sample by using electrostatic lenses.

These two diffraction techniques are described hereafter at point E and F. Before that, the general diffraction conditions and the lateral and in depth properties are discussed.

III.2.B. Diffraction conditions

For simplicity, the diffraction condition can be determined in a one dimensional case and then generalized to the three dimensional case. Let's consider Figure III-1 with a one dimensional network of atoms with a spacing a between two adjacent atoms. The direction of the incident and diffracted beams is respectively θ_i and θ_f with respect to the normal to the surface. The incident beam is characterized by a wave vector $k_i = 2\pi/\lambda_i$ and the diffracted beam by a wave vector k_f . In the case of elastic scattering, momentum is conserved and $k_i = k_f = k$. Constructive interference between the diffracted beams occurs if the optical path of two adjacent beams differs by an integer number of wavelengths associated to the electrons:

$$a \sin \theta_f - a \sin \theta_i = n\lambda \text{ with } n \in \mathbb{Z} \quad (3.6)$$

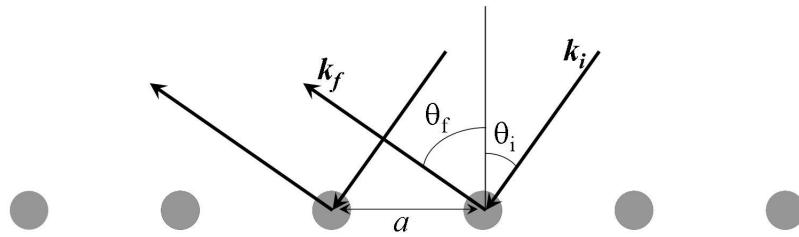


Figure III-1. Schematic of the incident beam diffraction.

Introducing the wave vector k in this equation leads to the following constructive interference condition of diffraction:

$$k (\sin \theta_f - \sin \theta_i) = n \frac{2\pi}{a} \quad (3.7)$$

$$k_{f\parallel} - k_{i\parallel} = n \frac{2\pi}{a}$$

To generalize this equation and to take into account the fact that the electrons interact only with the first layer of the crystal, the real space can be considered as a set of points in a 2D

plane. The Ewald sphere construction can be used to determine the diffraction condition in this 2D case.

If the real surface is the (100) orientation of a diamond structure, two orthogonal basis vectors \mathbf{a} and \mathbf{b} can generate the whole surface. From these vectors, the reciprocal space basis vectors \mathbf{a}^* and \mathbf{b}^* generate the related 2D mesh (Figure III-2a).

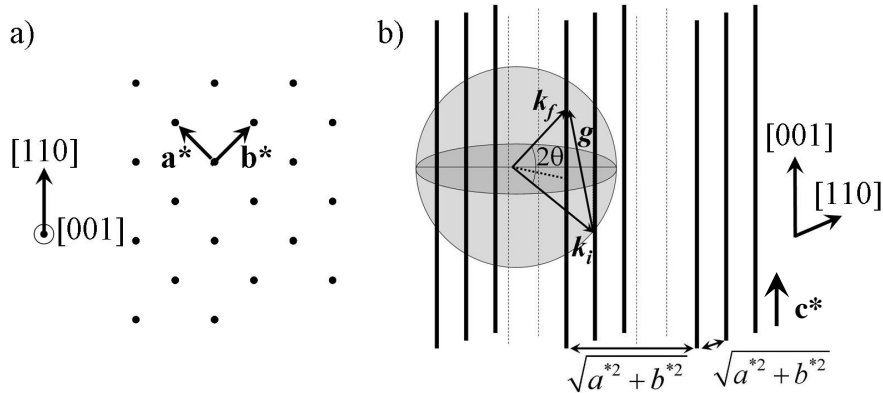


Figure III-2. Reciprocal lattice of the (100) surface of the face-centered cubic structure. a) Top view and b) side view with the Ewald sphere represented.

The reciprocal space is a set of parallel rods spaced by a distance $2\pi/a$ and $2\pi/b$. These rods are not infinitely thin because of the thermal vibration of the atoms in real space around the equilibrium position and because of the defects in the crystal surface.

An elegant way to deduce the diffraction condition for the constructive interference is to construct the Ewald sphere [20]. The incident beam is parallel to a wave vector \mathbf{k}_i and the diffracted beam to a wave vector \mathbf{k}_f . Energy and momentum conservation implies that these two vectors have the same norm. The vector \mathbf{k}_i is chosen so that its end corresponds with a node of the reciprocal space. In the case of a reciprocal space made of rods, any point along a rod can be chosen. A sphere of radius k_i can be drawn, centered at the origin of the \mathbf{k}_i vector. All the \mathbf{k}_f vectors with the same origin that the \mathbf{k}_i vector and whose end corresponds with a rod of the reciprocal lattice determine the conditions to observe a constructive interference (Figure III-2b). The angle between \mathbf{k}_i and \mathbf{k}_f is called 2θ . By changing the energy of the incident electron beam, the norm of the \mathbf{k}_i vector is changed and hence the radius of the Ewald sphere is modified. As a consequence, constructive interference is observed for different angles. In Figure III-2, the vector \mathbf{g} is defined as $\mathbf{g} = \mathbf{k}_f - \mathbf{k}_i$. The Ewald sphere construction implies that constructive interference occurs if \mathbf{g} connects two points existing in the reciprocal

space, hence $\mathbf{g} = h\mathbf{a}^* + k\mathbf{b}^* + l\mathbf{c}^*$. The notation (hkl) is often used to indicate the end of the vector \mathbf{g} and the origin (000) is positioned at the end of the vector \mathbf{k}_i and is called the specular spot. If the reciprocal space is a set of dots in 2D (with rods in the \mathbf{c}^* direction like in Figure III-2), h and k are integer numbers and l is a real number. If the reciprocal space is a set of points in 3D (with dots also in the \mathbf{c}^* direction), h , k and l are integer numbers.

In the case of a face-centered cubic structure, we can write that $a = b = c$ and $a^* = b^* = c^*$ and the condition for constructive interference can be deduced as follows:

$$\sin \theta = \frac{|\mathbf{g}|/2}{|\mathbf{k}_i|} = \frac{1/2 \sqrt{\left(h \frac{2\pi}{a}\right)^2 + \left(k \frac{2\pi}{b}\right)^2 + \left(l \frac{2\pi}{c}\right)^2}}{2\pi/\lambda} = \frac{\lambda \sqrt{h^2 + k^2 + l^2}}{2a} \quad (3.8)$$

This equation is known as the Bragg relation.

III.2.C. Penetration depth of the electron beam

Electrons are charged particles interacting strongly with matter. The inelastic mean free path (IMFP) of the electrons is defined as the average distance travelled before losing all or part of their kinetic energy because of an inelastic collision. This distance is a function of the initial kinetic energy and the absorbing material.

Tanuma *et al.* [21] analyzed the experimental values of the IMFP for organic materials to develop an equation to estimate the IMFP (λ) of other materials (organic and inorganic). This model is called TPP-2M and the IMFP in nm is given by:

$$\lambda(E) = \frac{0.1 E}{E_p^2 \left[\beta \ln(\gamma E) - (C/E) + (D/E^2) \right]} \quad (3.9)$$

with the following parameters:

$$\begin{aligned} U &= N_v \rho / M \\ E_p &= 28.8 \sqrt{U} \\ \beta &= -0.10 + 0.944 \left(E_p^2 + E_g^2 \right)^{-1/2} + 0.069 \rho^{0.1} \\ \gamma &= 0.191 \rho^{-1/2} \\ U &= N_v \rho / M \\ C &= 1.97 - 0.91 U \\ D &= 53.4 - 20.8 U \end{aligned} \quad (3.10)$$

E_p is the plasmon energy (in eV), N_v is the number of valence electrons per atom or molecule (given in [21]), ρ is the density (in g/cm³), M the atomic or molecular mass (in g), E_g the bandgap energy (in eV) and E the kinetic energy of the electron (in eV). In Figure III-3, the IMFP is represented for Si, CdTe and ZnTe.

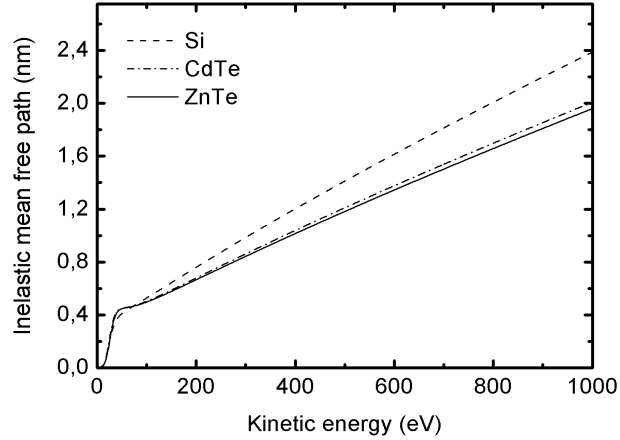


Figure III-3. IMFP of electrons (λ) as a function of the kinetic energy.

III.2.D. Coherence length of the beam

The LEED and RHEED patterns are representative of the surface crystallinity. However, the probed area is not defined by the size of the electron beam, but the coherence length of the beam. It is defined as the maximum spatial area where the interference phenomena can occur between two diffracted beams. This means that the complex amplitude of the diffracted electrons (taking into account the spatial amplitude and the phase) can be added only inside the coherence length of the beam. The size of the incident beam on the sample can be seen as the juxtaposition of circular domains with a diameter equal to the coherence length. The final diffraction pattern is the superposition of the patterns created by each domain.

The coherence length of a beam can be determined by taking into account two experimental limitations [22-24]: the dispersion of the wavelength (L_λ) leading to lack of precision in the direction parallel to the beam and the focusing of the incident beam (L_θ) creating an error in the direction perpendicular to the beam. Because of the normal incidence in LEED and the grazing incidence in RHEED, L_θ is the limiting factor for LEED and L_λ for RHEED. The imprecision of the wavelength has an influence on the Ewald sphere: the thickness of the external surface of the sphere is not infinitely thin, but a thickness Δk needs to be taken into account.

L_λ and L_θ can be calculated by considering electrons propagating in the x direction and modeled by a plane wave $e^{ik_i x}$ with a wave vector distribution centered on k_i and with a dispersion Δk due to experimental imperfections. According to elementary quantum physics theory [25], the wave function associated with the electrons can be written as:

$$\psi(x) = \frac{1}{\sqrt{2\pi}} \int_{-\infty}^{+\infty} g(k) e^{ikx} dk \quad (3.11)$$

An example for $g(k)$ is a function shown in Figure III-4 and represents the distribution of the wave vectors around an average of k_i . Because of the domain of existence of $g(k)$, the integral can be roughly approximated by the sum of three terms: a plane wave centered on k_i with an amplitude A and two plane waves with a wave vector of $k_i - \Delta k/2$ and $k_i + \Delta k/2$ whose amplitude is $A/2$. The wave function can be rewritten as:

$$\psi(x) = \frac{A}{\sqrt{2\pi}} e^{ik_i x} \left[1 + \cos\left(\frac{\Delta k}{2} x\right) \right] \quad (3.12)$$

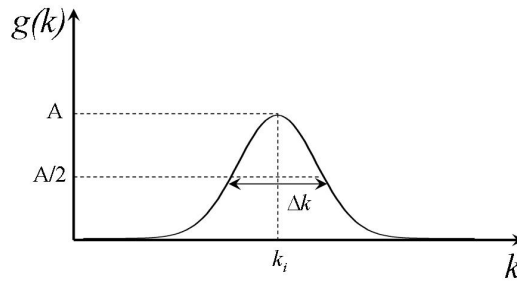


Figure III-4. Example for the distribution of the wave vectors.

This wave function can be generalized for a propagation direction \mathbf{r} in 3D:

$$\psi(\mathbf{r}) = \frac{A}{\sqrt{(2\pi)^3}} e^{ik_i \cdot \mathbf{r}} \left[1 + \cos\left(\frac{\Delta \mathbf{k} \cdot \mathbf{r}}{2}\right) \right] \quad (3.13)$$

This amplitude is maximum when $\mathbf{r} = 0$ and is zero when the phase difference between the vector \mathbf{k}_i and $\mathbf{k}_i - \Delta \mathbf{k}/2$ or $\mathbf{k}_i + \Delta \mathbf{k}/2$ is respectively π or $-\pi$. These destructive interferences appear when $\mathbf{r} = \pm \Delta \mathbf{r}/2$ where $\Delta \mathbf{r}$ is linked to $\Delta \mathbf{k}$ by the expression: $\Delta \mathbf{r} \cdot \Delta \mathbf{k} = 4\pi$. From this expression, the general definition of the coherence length (L_C) can be determined:

$$L_C = \frac{4\pi}{\|\Delta \mathbf{k}\|} \quad (3.14)$$

From this equation, L_λ and L_θ can be estimated:

- The spatial coherence length (L_λ) is obtained when considering the relation between the wave vector ($k_i = k_f = k$) and the energy (E) of the beam. For an electron beam of

energy $E = \frac{\hbar^2 k^2}{2m_e}$, the derivative of this expression gives an equation for the dispersion in energy:

$$\frac{\Delta E}{\Delta k} = \frac{\hbar^2 k}{m_e} \quad (3.15)$$

This means that there is a correlation between the dispersion of energy and the dispersion of the wave vector. Combining equations (3.5), (3.14) and (3.15), the spatial coherence length is given by:

$$L_\lambda (\text{nm}) = \frac{4\pi}{\Delta k} = \frac{4\lambda E}{\Delta E} = 4.92 \frac{\sqrt{E(\text{eV})}}{\Delta E(\text{eV})} \quad (3.16)$$

- The angular coherence (L_θ) is found by considering the electron beam as a cone with an angular aperture of $\frac{\Delta\theta}{2}$. In the direction perpendicular to the beam, the widening of the wave vector is (for small angular aperture expressed in radians):

$$\Delta k = 2k \sin \frac{\Delta\theta}{2} = k \cdot \Delta\theta \quad (3.17)$$

Combining equations (3.5), (3.14) and (3.17), the angular coherence length L_θ is:

$$L_\theta (\text{nm}) = \frac{2\lambda}{\Delta\theta} = \frac{2.46}{\Delta\theta \cdot \sqrt{E(\text{eV})}} \quad (3.18)$$

III.2.E. Low energy electron diffraction (LEED)

Low energy electron diffraction uses an electron gun to irradiate the surface of the sample in normal incidence. Diffraction of the electron beam by the surface is possible if the wavelength associated to the electrons is comparable to the lattice parameter of the crystalline surface. According to equation (3.5), an initial energy between 30 and 100 eV is associated with a wavelength between 0.225 and 0.123 nm, of the order of magnitude of the interatomic distance. According to Figure III-3, electrons of such energy are characterized by a penetration depth of about 5 Å, making LEED extremely surface sensitive.

In our system, electrons are emitted from a LaB₆ filament heated up to 1700 K. The electrons are accelerated by a potential difference applied between the filament and the sample and they are focused on the sample by a set of electrostatic lenses. The elastically diffracted electrons

are collected on a phosphorescent screen set at 5 kV. A 4 grid system is used to stop inelastically scattered and secondary electrons which would create a background on the screen and to collect the elastically diffracted electrons on an observation screen (Figure III-5): grid 4 is grounded so that the electric field around the grounded substrate is zero. Grids 2 and 3 act as a filter for the diffracted electrons: a potential difference is applied between the two grids to create a retarding electric field. Hence, the secondary electrons (with a small kinetic energy) are repulsed and will not create a background on the screen. The elastically diffracted electrons with a kinetic energy equals to the energy of the incident beam are retarded because of the presence of the electric field but they can go through the retarding system. The grid 1 is grounded, hence the potential difference between this grid and the screen creates an accelerating electric field when applied to the elastically diffracted electrons emerging from the retarding system.

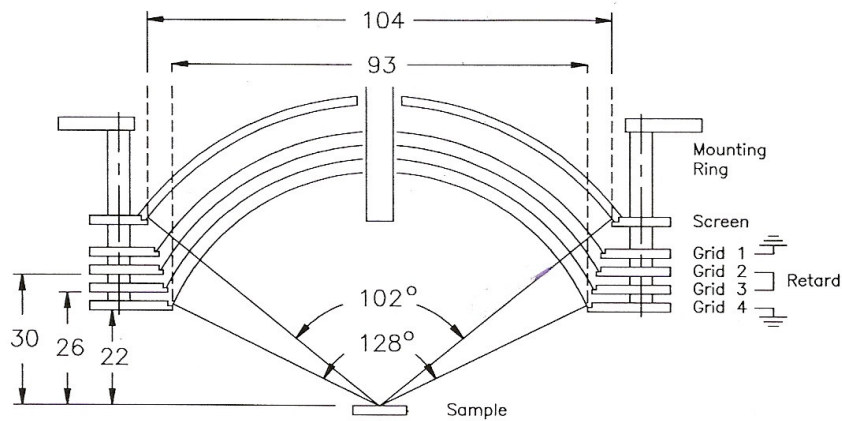


Figure III-5. Schematic of the 4 grid LEED system by Omicron Nanotechnology.

From equations (3.5) and (3.6) and because of the normal incidence of the incident beam ($\theta_i = 0$) the mathematical expression for the diffraction condition becomes:

$$a \text{ (nm)} = \frac{1.23}{\sqrt{E \text{ (eV)}}} \cdot \frac{n}{\sin \theta_f} \quad \text{with } n \in \mathbb{N}_0 \quad (3.19)$$

θ_f can be measured as follows. A picture of the diffraction pattern is taken, large enough to show the entire screen. The distance x' from the center of the screen and a diffraction spot and the diameter of the screen D' can be measured directly on the picture (Figure III-6). Knowing the real diameter of the screen D , one can calculate the real distance x . Assuming that the sample is at a distance d from the optical center of the screen and noting R the spherical radius of the screen, θ_f is given by (Annex 1):

$$\theta_f = \arctg\left(\frac{x}{\sqrt{R^2 - x^2 - d}}\right) \quad (3.20)$$

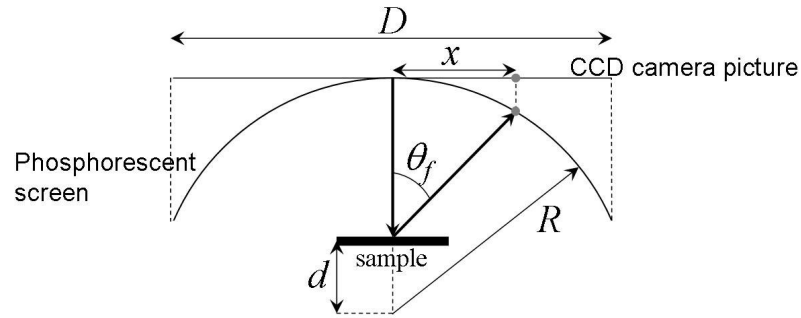


Figure III-6. LEED parameters to measure θ_f .

At the Laboratory of Physics of Electronic Materials (LPEM), the UHV chamber is equipped with a SpectaLEED system from Omicron Nanotechnology (Figure III-7). The technical data are presented in Table III-1. From the calculation of the lattice parameter of a Si(111) unreconstructed surface as reference from a LEED diffraction pattern, we determined that the sample is positioned at 4 mm beyond the optical center of the LEED system (i.e. $d = -4$ mm in the equation (3.20)) and the screen is characterized by a spherical radius R of 66 mm and a diameter D of 104 mm.



Figure III-7. SpectaLEED.

	Spherical radius	Circular diameter	Aperture angle
Screen	66 mm	104 mm	102°
Grid 1	60 mm	99 mm	110°
Grid 2	57 mm	97 mm	115°
Grid 3	54 mm	95 mm	122°
Grid 4	51 mm	93 mm	128°

Table III-1. Technical data of the SpectaLEED.

If the sample surface is perpendicular to the direction of the incident beam, the coherence length of the beam is limited by its divergence (resulting in a Δk parallel to the surface). A typical value for the spread of the electron beam in LEED is $\Delta\theta = 1$ mrad. According to

equation (3.18), the coherence length of the beam for electron energy between 30 and 100 eV varies respectively from 450 to 250 nm.

In this thesis, the growth of CdTe is performed on a Si(211) substrate. As explained earlier, Si(211) surface is not a flat surface, but composed of Si(111) and Si(100) terraces. These terraces make an angle of 19.47 and 37.26° with respect to the (211) plane of the substrate. The incident beam then makes an angle α_1 of 109.47° with respect to the (111) terrace and an angle α_2 of 127.26° with respect to the (100) terrace. The total coherence length on a surface made of terraces needs to consider both the angular and the spatial spreading of the beam. Denoting by α the angle between the incident beam and the surface, the coherence length in the plane of the surface can be calculated as:

$$L_c \text{ (nm)} = \frac{4.92 \sqrt{E}}{2.E.\Delta\theta|\sin \alpha| + \Delta E.|\cos \alpha|} \quad (3.21)$$

The graph in Figure III-8 represents this equation and is drawn considering a $\Delta\theta = 1$ mrad, an energy resolution $\Delta E = 0.1$ eV and a primary beam energy of 30, 65 and 100 eV. α represents the angle between the incident beam and the really probed surface. The specific angles for the (211) orientation are denoted α_1 and α_2 in the figure. A coherence length of 300 and 250 nm respectively for the (111) and (100) terraces can be calculated for an incident beam characterized by an energy of 30 eV.

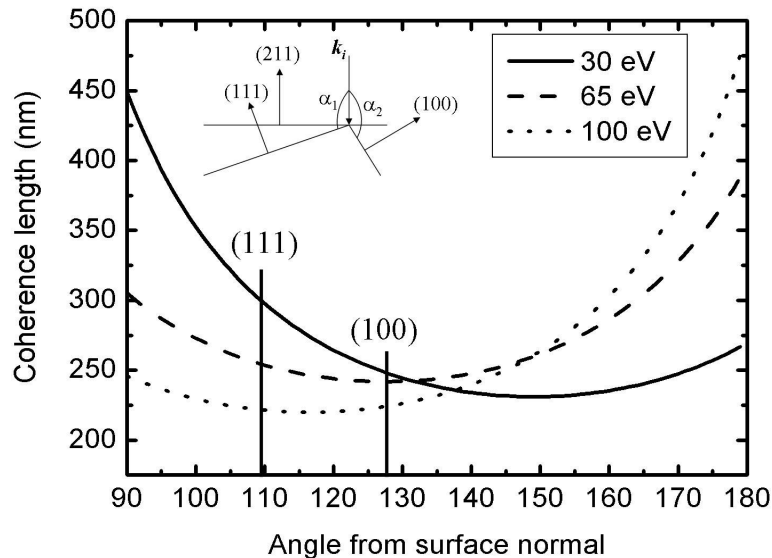


Figure III-8. Coherence length in LEED.

III.2.F. Reflection high energy electron diffraction (RHEED)

The main disadvantage of LEED is that the incident beam is in normal incidence, it is thus impossible to use this technique to monitor in real time the crystallinity during epitaxial growth because the evaporation cells are in principle placed in front of the substrate. RHEED can avoid this problem: the incident beam is sent in grazing incidence and the reflected beam is collected on a phosphorescent screen placed in the direction opposite from the electron gun. This geometry insures that the entire space in front of the substrate is available for evaporation cells (Figure III-9).

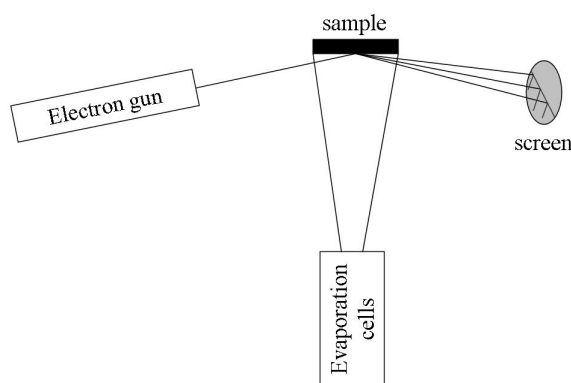


Figure III-9. RHEED geometry.

In RHEED, the electrons have an energy between 10 and 50 keV corresponding to a wavelength between 0.123 and 0.055 Å. Even with this high energy, the RHEED is still a surface analysis technique because of the grazing incidence angle [26]. For a beam of 10 keV and an angle of incidence of 2°, the penetration depth in silicon is only 0.4 nm. Hence, for the diffraction conditions, it is only necessary to work in two dimensions in the reciprocal space.

The electrons diffracted elastically on the surface interfere in a constructive way under particular angles, producing bright spots or streaks on the screen. Inelastically scattered electrons produce a diffuse background on the screen. At high energy, the probability of inelastic scattering is low. Thus if the surface is highly crystalline, the diffraction pattern observed on the screen is highly contrasted.

In comparison with LEED, the associated wavelength of the electrons is 10 to 100 times smaller, thus the radius of the Ewald sphere is 10 to 100 times larger. If the sample surface is perfect (free of defects and infinitely thin rods in the reciprocal lattice due to the absence of atomic vibrations), the intersection between the Ewald sphere and the rods of a 2D reciprocal

lattice is set of points (Figure III-10a). However, two phenomena modify this hypothesis of perfection [27]:

- The rods of the reciprocal lattice are not infinitely thin because of the thermal vibration of the atoms in real space and because of the presence of defects on the surface (Figure III-10b);
- The incident electron beam has an angular and a spatial spreading resulting in non-zero thickness of the Ewald sphere (Figure III-10c).

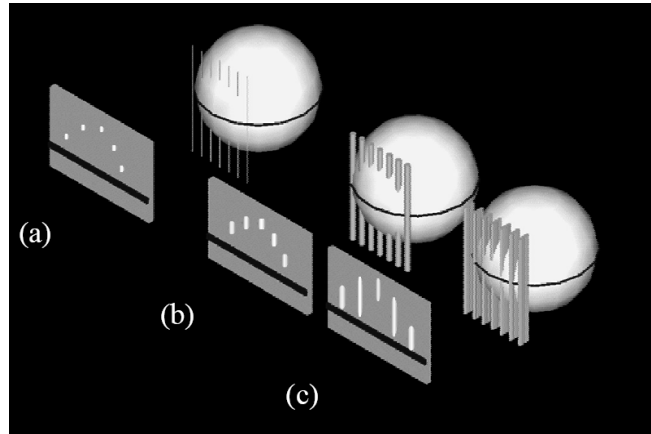


Figure III-10. RHEED pattern of a flat surface with a) perfect reciprocal lattice rods and Ewald sphere; b) perfect Ewald sphere; c) real case.

Hence, the intersection between the Ewald sphere and the reciprocal rods is a set of streaks for a perfectly flat surface.

If the incident is in grazing incidence, the coherence length is limited by the Δk component parallel to the beam (i.e. the spatial spread of the beam). Using equation (3.16) with a beam energy spread of about 1 eV, a coherence length of about 500 nm can be calculated for a 10 keV energy beam and in the direction of the k_i vector. Because of the small incidence angle (typically between 1 and 4°), the coherence length in the plane of the surface is only modified by the cosine of this angle. In first approximation, one can consider that the previously calculated coherence length is the same for the surface of the sample.

For the (211) orientation, this coherence length is decreased because of the real angle of incidence on this tilted surface, as presented in the schematic of Figure III-11. If the incident beam hits the (211) surface with an angle of 1°, the angle of incidence on the (111) and (100) terraces is respectively $\alpha_1 = 20.47^\circ$ and $\alpha_2 = 38.26^\circ$. In this case, the coherence length is a

consequence of both spatial and angular spread of the incident beam and equation (3.21) is used to draw the coherence length as a function of the angle α between the incident beam and the analyzed surface. Figure III-11 is obtained when considering an electron beam of 10, 30 and 50 keV with an energy spread of 1 eV and an angular spread $\Delta\theta = 1$ mrad. For α_1 and α_2 , the coherence length is respectively of 60 and 35 nm for an incident beam energy of 10 keV. A beam with an incident energy of 100 eV is also drawn to check that in this case, the coherence length in normal incidence (i.e. $\alpha = 90^\circ$) is the same that the coherence length obtained in the LEED study (Figure III-8) for the same angle.

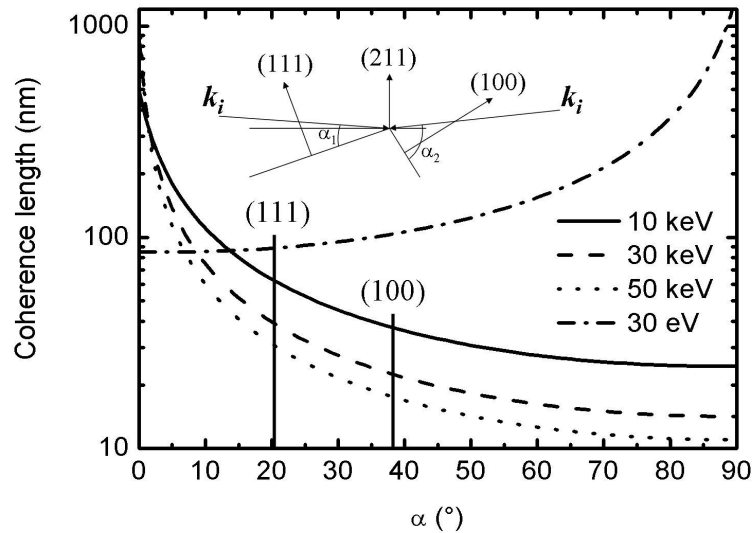


Figure III-11. Coherence length in RHEED.

The lattice parameter of a sample can be measured by RHEED. As an example, we consider a simple cubic structure with the two basis vectors \mathbf{a}^* and \mathbf{b}^* generating the 2D reciprocal space probed by the electron beam (Figure III-12). The wave vector of the incident electron beam is \mathbf{k}_i and is drawn so that its end corresponds with a node of the reciprocal space. The end of the \mathbf{k}_i vector corresponds to a rod labeled (00) in the $(\mathbf{a}^*, \mathbf{b}^*)$ basis. The Ewald sphere can then be drawn, revealing the possible ending points of diffracted beams characterized by \mathbf{k}_f vectors. The point S is called the specular spot and corresponds to a diffracted beam in the plane containing the incident beam and perpendicular to the surface. The sample is at a distance L from the screen and the distance between two streaks is denoted l . If L is much bigger than l :

$$\tan(2\theta) = \frac{l}{L} \cong 2\theta \quad (3.22)$$

From equation (3.8), considering the small angle approximation and because \mathbf{k}_i and \mathbf{k}_f are both nearly with a null component perpendicularly to the surface (so that the length along the \mathbf{c}^* axis in reciprocal space is approximated to be zero), the lattice parameter in real space is:

$$a(nm) = \frac{\lambda(nm)\sqrt{h^2 + k^2}}{2\sin\theta} \cong \frac{\lambda(nm)\sqrt{h^2 + k^2}}{2\theta} \quad (3.23)$$

Combining equations (3.22) and (3.23):

$$a(nm) = \frac{\lambda L \sqrt{h^2 + k^2}}{l} \quad (3.24)$$

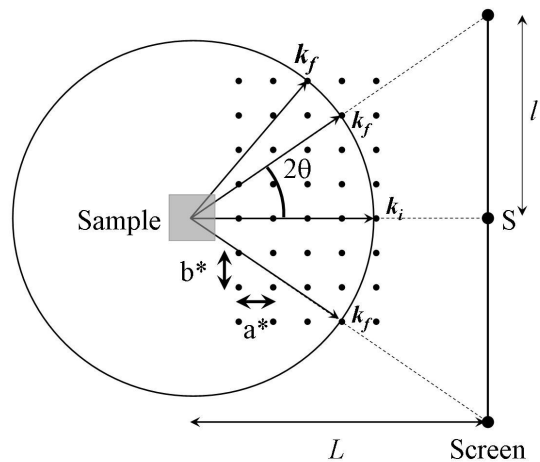


Figure III-12. Ewald construction for RHEED.

III.3. X-ray diffraction techniques

If the bulk cristallinity of the sample has to be analyzed, X-rays are suitable because they are uncharged particles and characterized by a null mass; hence they weakly interact with the matter.

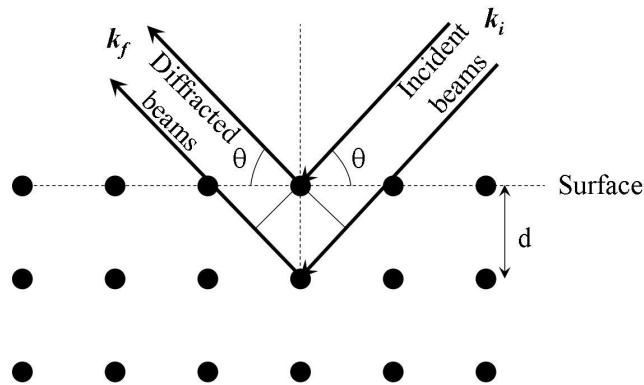


Figure III-13. Bragg-Brentano X-ray diffraction.

The constructive interference between diffracted beams is represented in Figure III-13. The experiment is carried out in the Bragg-Brentano geometry: the angle between the surface and the incident beam or the diffracted beam is the same (defined as θ in the figure). The interference between the diffracted beams is constructive if the optical path between two adjacent beams is equal to an integer number of the wavelength associated to the X-rays (Bragg diffraction condition):

$$2d \sin \theta = n\lambda \text{ with } n \in \mathbb{N}_0 \quad (3.25)$$

In this equation, d is the distance between two atomic planes.

This distance d is a function of the crystal orientation. For cubic structures, the lattice parameter is equal to the distance between two consecutive (100) planes (d_{100}). For a set of (hkl) planes in a cubic structure, the distance between two adjacent planes d_{hkl} is:

$$d_{hkl} = \frac{d_{100}}{\sqrt{h^2 + k^2 + l^2}} \quad (3.26)$$

One should keep in mind that for more complex crystalline structures (CdTe zinc blende or Si diamond structure), systematic extinctions occur so that some diffraction peaks cannot be observed by X-ray diffraction (see chapter II). For example, for CdTe(211), the (211) peak cannot be observed, but the (422) is allowed.

For constructive interference, the intensity of the diffracted beam is proportional to the squared Fourier transform of the electronic density [28]:

$$I(\mathbf{g}) \propto \left| \int \rho(\mathbf{r}) e^{i\mathbf{g} \cdot \mathbf{r}} d\mathbf{r} \right|^2 \text{ with } \mathbf{g} = \mathbf{k}_f - \mathbf{k}_i \quad (3.27)$$

The X-ray source consists of a copper cathode irradiated by an electron beam. The excited copper atoms stabilize by emitting three photons in the X-ray range. These photons are a signature of the $K_{\alpha 1}$, $K_{\alpha 2}$ and K_{β} lines of deexcitation (Figure III-14). A good interpretation of the X-ray diffraction spectra requires the creation of a monochromatic analysis beam in order to avoid the multiplication of the peaks. For this purpose and because of the important difference between the energy associated to the K_{β} line compared to the others, a foil of nickel can be inserted between the X-ray beam and the sample to absorb the K_{β} radiation. Hence, in X-ray diffraction (XRD), the incident beam is composed of two components related to the $K_{\alpha 1}$ and $K_{\alpha 2}$ lines with a characteristic associated wavelength of respectively $\lambda_1 = 1.540592 \text{ \AA}$ and $\lambda_2 = 1.544414 \text{ \AA}$ [29].

The width of a peak of diffraction can be influenced by the defect density (because of misfit dislocations or single defects) creating local variations in the lattice constant. In addition, the compressive or tensile strain created by a lattice and a thermal mismatches between the epilayer and the substrate can also result in a broadening of the peak of diffraction. From these considerations, XRD can be a suitable tool to characterize the crystalline quality of an epilayer. However, this requires a perfectly monochromatic probing beam to avoid a natural broadening due to the presence of multiple X-ray energies. As an example for a substrate of Si(100), if the incident beam is composed of the $K_{\alpha 1}$ and $K_{\alpha 2}$ lines and according to equation (3.25), diffraction is observed for 2 angles θ_1 and θ_2 separated by 0.04° (144 arcsec). Hence if the real width of the diffraction peak because of the influence of defects or strain is in this range, it is not possible to distinguish the factor responsible for the spread observed. So, one of the two K_{α} lines has to be suppressed in order to interpret the width of a diffraction peak. The problem is that it is not possible to remove one of the two components of the beam with an absorbing material because the energy difference between the associated photons is too small.

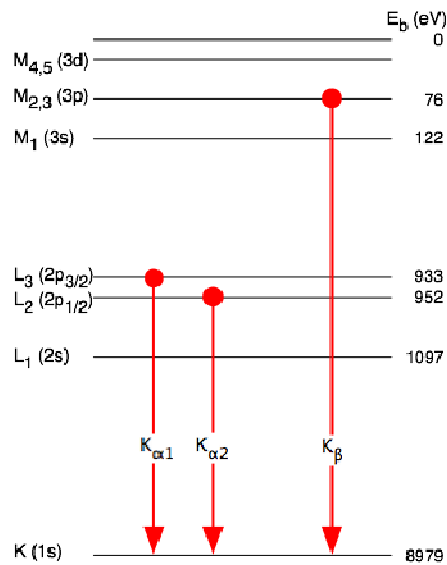


Figure III-14. Copper electronic transition diagram.

Double crystal rocking curve X-ray diffraction (DCRC-XRD) is a technique developed to suppress one of the two lines of the incident beam (Figure III-15). The incident beam (whose K_{β} line has been filtered by the nickel foil) is firstly sent on a reference crystal (for example Ge(331)) with a very high crystalline quality (very low defect density, leading to a full width at half maximum (FWHM) of the diffraction peak inferior to 10 arcsec). Because of the high

Miller indices of the germanium crystal, a splitting of the 2 diffracted beams is observed (see equations (3.25) and (3.26)): 0.10° between the X-rays of the $K_{\alpha 1}$ and $K_{\alpha 2}$ lines of copper. Hence a spread of the beam is observed after the first crystal. A slit can then be introduced between the reference crystal and the sample in order to suppress one of the two components. The result is that a monochromatic beam is sent on the sample to be analyzed. Because of the lower intensity of the $K_{\alpha 2}$ line, the X-rays from the $K_{\alpha 1}$ line are selected to probe the sample.

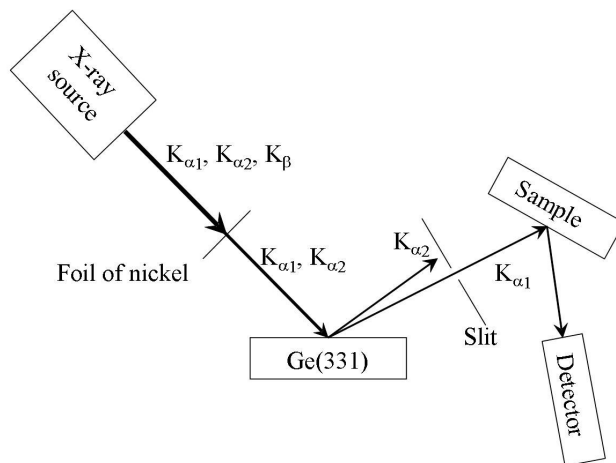


Figure III-15. DCRC-XRD principle.

III.4. Photoemission electron microscopy (PEEM)

III.4.A. Working principle

In photoemission electron microscopy, the sample is illuminated by a UV source (typically a mercury vapor lamp, a helium lamp or a synchrotron radiation) and an image of the spatial distribution of the photoelectrons is produced on a fluorescent screen. The microscope is composed of a set of electrostatic lenses (to focus and to magnify the image) and an imaging system to accelerate and to focus the photoelectrons on an observation screen. The basic principle is illustrated in Figure III-16a [30].

Photoelectrons emitted from the sample are accelerated by an extraction potential towards a multichannel plate (MCP) where the electronic signal is amplified. The amplified amount of electrons is accelerated to a fluorescent screen where real-time observation is possible.

The PEEM is composed of 4 stages: a set of objective lenses (sample, column, extractor and focus), a contrast aperture, an octupole for deflection and stigmatism of the beam and two projective lenses for magnification.

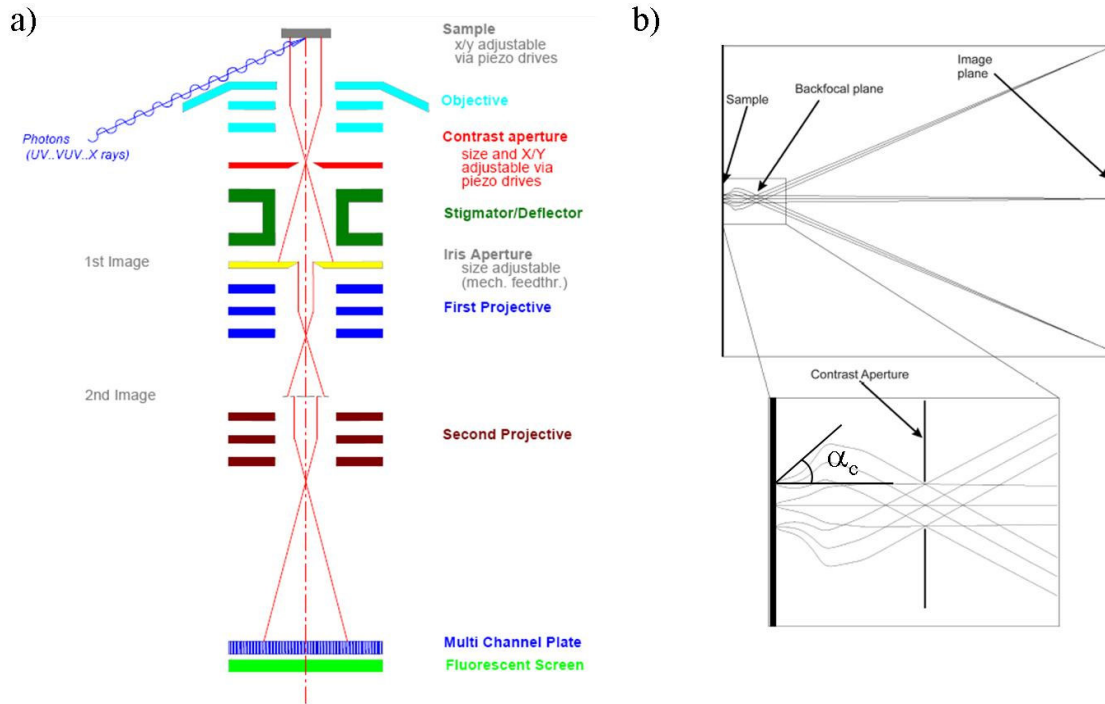


Figure III-16. a) Basic principle of PEEM; b) Trajectory of the electrons close to the contrast aperture.

The objective lenses are used to accelerate the photoelectrons and to focus them on the MCP. The extractor potential is typically set to 15 kV. Higher potential leads to better resolution.

The contrast aperture (Figure III-16b) is used to optimize the resolution by decreasing the critical angle of emission (α_c) of the collected electrons. But if the angle is decreased, the collected intensity is reduced. A compromise has to be found between resolution and intensity.

The octupole can suppress the obliquity and spherical aberrations (by using the stigmatism lenses) and can move the field of view (via the deflection lenses).

The projective lenses are used to magnify the image. An iris aperture is placed between the octupole and the projective lenses to suppress the marginal beams which can influence the resolution when the magnifying projective lenses are used.

In addition to the spherical and obliquity aberrations stated above, further loss of resolution can be due to vibrations between the sample and the microscope. This can be avoided by attaching the sample stage to the microscope.

Under optimal conditions, the limitation in the resolution is mainly due to the chromatic aberration of the electrostatic lenses system [31].

The UV source used at the LPEM is a mercury vapor lamp with a photon energy of 4.9 eV. If the sample is an intrinsic semiconductor, the electrons emitted by photoelectric effect are coming from the valence band because of the low energy of the incident beam. The extraction of an electron is possible if the sum of the work function (ϕ) and the difference between the top of the valence band (VB_{max}) and the Fermi level (E_f) is inferior to the photon energy $h\nu$ (Figure III-17). In this case, the electrons can reach the vacuum level before being accelerated by the extraction voltage.

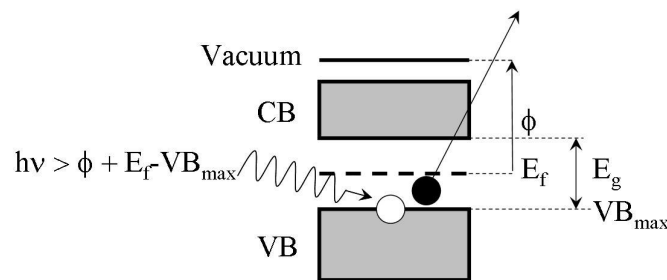


Figure III-17. Photoemission process in PEEM.

The intensity contrast observed on the screen is a function of the number of electrons collected by the MCP. Several factors can influence the number of electrons (and then the intensity):

- Non uniform work function due to the presence of different chemical species;
- Defects or steps modifying the work function of a single element;
- Different crystalline orientations;
- Topographic effects.

III.4.B. Aberrations of electrostatic lenses

Figure III-18 shows a schematic representation of the first stage of the PEEM. The sample is close to the extractor (real sample). The strong electric field bends the electron trajectory towards the surface normal. Depending on the diameter of the contrast aperture, the angle α is

modified. In the absence of the extractor lens, the collected electrons can be seen as emitted from a virtual sample placed behind the real sample, under an angle α' . In other words, in the absence of the strong electric field created by the extraction potential, the electrons propagate as if they were emitted under an angle α' from a virtual sample placed behind the real sample.

The electrostatic lenses cause loss of resolution due to three different types of aberration: chromatic, spherical and aberration of diffraction.

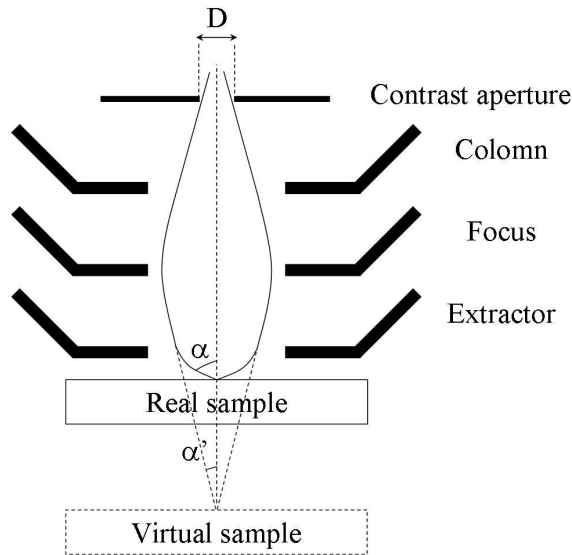


Figure III-18. Aberration parameters for electrostatic lenses.

Aberration depends on the angle α' and can be approximated by the following formulae:

$$\text{Chromatic aberration: } d_c = 4.f.\frac{\Delta E}{E}.\alpha'$$

$$\text{Spherical aberration: } d_s = 5.f.(\alpha')^3 \quad (3.28)$$

$$\text{Aberration of diffraction: } d_d = \frac{\lambda}{2\alpha'}$$

f is the focal length of the tetrode lens composed of the sample, the extractor, the focus and the column; E and ΔE are respectively the photon energy (4.9 eV for the Hg lamp) and the width of this emission line (2 meV) and λ is the wavelength of the electrons with a kinetic energy of 15 keV at the exit of the extractor (coinciding with the entrance of the contrast aperture).

The relationship between the diameter of the contrast aperture (D) and α' can be calculated (see Annex 2 for more details):

$$\alpha' = 119.D \quad (3.29)$$

Using equations (3.28), the total lateral resolution (d) can be drawn as a function of d_c , d_s and d_d (Figure III-19):

$$d = \sqrt{d_c^2 + d_s^2 + d_d^2} \quad (3.30)$$

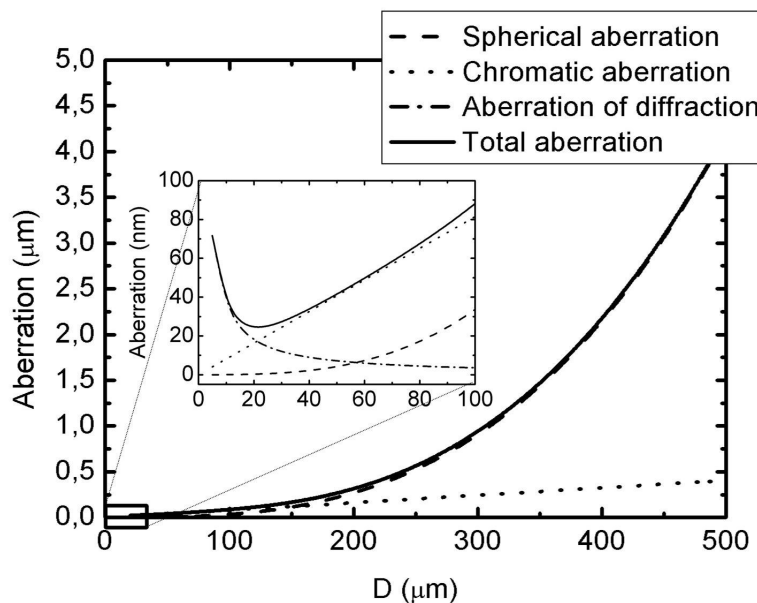


Figure III-19. Spherical aberration (dashed line), chromatic aberration (dotted line), aberration of diffraction (dash-dotted line) and total aberration (solid line) as a function of the contrast aperture diameter D .

The available contrast apertures have a diameter of 30, 70, 150, 500 and 1500 μm . The highest achievable resolution of 27 nm is obtained with the smallest aperture and is mainly limited by chromatic and diffraction aberrations. However, if the image is observed without using the magnification lenses, a contrast aperture of 150 μm is required to observe the entire field of view on the sample. The related maximum lateral resolution is 165 nm and is caused mainly by the spherical aberration.

III.5. Auger electron spectroscopy (AES)

The core electronic structure of atoms is a signature which is different for each element of the periodic table. To probe the chemical composition of a sample, an incident beam of electrons is focused on the sample to eject an electron from the core level of an atom of the surface. The excited atom can be stabilized by emitting an electron from an upper energy level (Auger effect). In Auger electron spectroscopy (AES), this electron is collected and depending on its

kinetic energy, the chemical nature of the sample can be determined. The details of the Auger effect are presented in Annex 3.

III.5.A. Experimental facility

The excitation source is an electron beam with a primary energy between 3000 and 5000 eV. The beam is sent in normal incidence on the sample. Auger electrons of interest in this study have a kinetic energy below 1000 eV so the expected mean free path and the probed depth are therefore limited to several nanometers. Auger electrons emitted with an angle of 42.3° from the surface normal enter in a cylindrical mirror analyzer (CMA 100 provided by Omicron Nanotechnology) where they are energy filtered by tuning the potential of the cylinders composing the CMA. The electrons emerging from the CMA enter a channeltron electron multiplier (CEM) where the signal is amplified via an avalanche process. The energy resolution of the CMA is 0.5 %.

III.5.B. Depth emission

Auger electrons interact with matter before escaping from the sample to reach the analyzer. Only electrons emerging from the surface under an angle of $\theta = 47.7^\circ$ from the surface can be detected by the CMA. If I_0 is the intensity of an Auger line associated with electrons detected from a semi-infinite sample, the detected signal $I(d)$ for electrons emitted from a layer located between the surface and a depth d is (Figure III-20):

$$I(d) = I_0 \left(1 - e^{-\frac{d}{\lambda \sin \theta}} \right) \quad (3.31)$$

where λ is the mean free path of electrons determined on Figure III-3 for a given Auger electron kinetic energy.

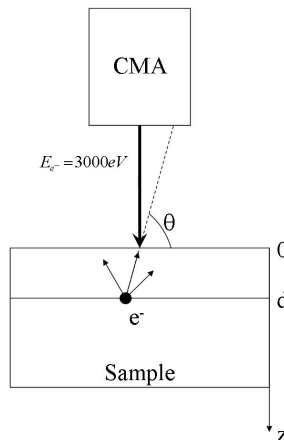


Figure III-20. AES geometry.

The ratio between I_0 and $I(d)$ is presented in Figure III-21: 95% of the maximum signal is due to electrons emitted within a depth of 3λ from the surface. Hence AES is surface sensitive.

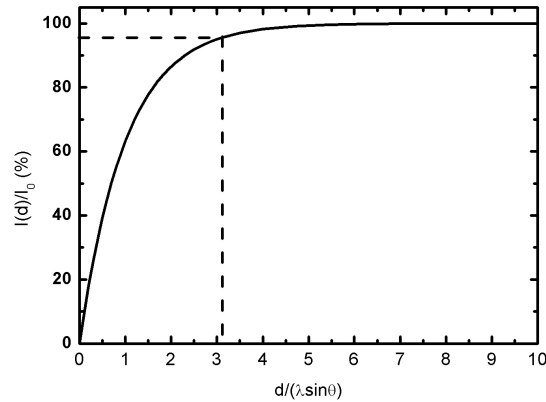


Figure III-21. Proportion of the maximum detected intensity as a function of the probed depth.

III.6. Molecular beam epitaxy chamber (MBE)

Molecular beam epitaxy (MBE) is used during this PhD thesis to grow the layers of CdTe(211)B/ZnTe(211)B/As/Si(211) and to study the feasibility of selective growth with this particular growth technique. MBE growth was first realized by Cho to grow GaP on CaF₂(111) [32]. The numerous advantages of MBE make it the ideal candidate to grow monocrystalline multilayers of very high quality:

- Control of the concentration ratio between the evaporated elements;
- Accurate control of the deposition time, leading to sharp interfaces between the layers;
- Control of the growth rate to ensure a monocrystalline structure of very high quality;
- Low temperature growth, avoiding the diffusion between the deposited layers.

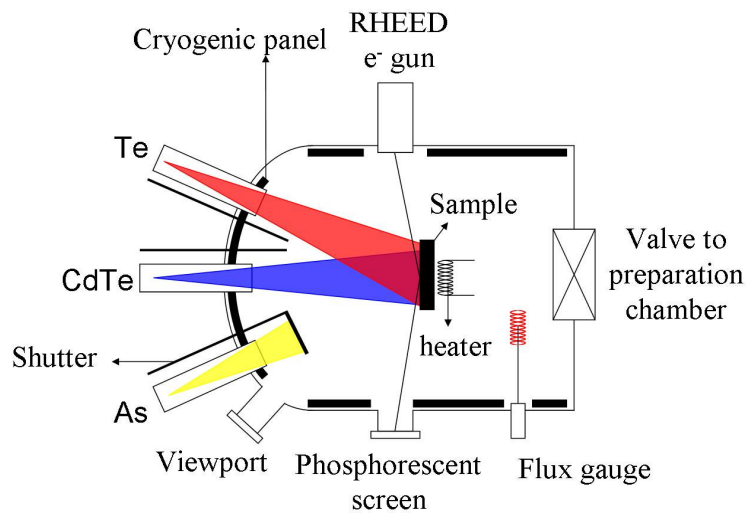


Figure III-22. Schematic of a MBE chamber.

A schematic drawing of a MBE chamber is presented in Figure III-22. Evaporation cells consist of pyrolytic boron nitride crucible containing the material to be evaporated. The cells are radiatively heated by tantalum filaments. Thermal shields surround the filament and the crucible in order to minimize heat losses (Figure III-23). The temperature is measured by a thermocouple attached close to the crucible. Stable crucible temperature is achieved by PID regulation to ensure a constant evaporation flux. Remote-controlled shutters can interrupt the evaporating flux in a fraction of second.

The base pressure of the MBE chamber is below $5 \cdot 10^{-10}$ mbar. During the growth, liquid nitrogen cools the cryogenic panels surrounding the cells and the MBE walls. These panels act as cold traps for the residual molecules present in the chamber when a shutter is quickly closed. A pressure gauge is positioned behind the sample to measure the vapor pressure and to give a rough idea of the deposition rate on the substrate. The MBE chamber is equipped with RHEED in order to monitor in-situ and in real time the crystallinity and the growth rate of the sample. In our experiments, the RHEED electron gun is operated at 10 keV.

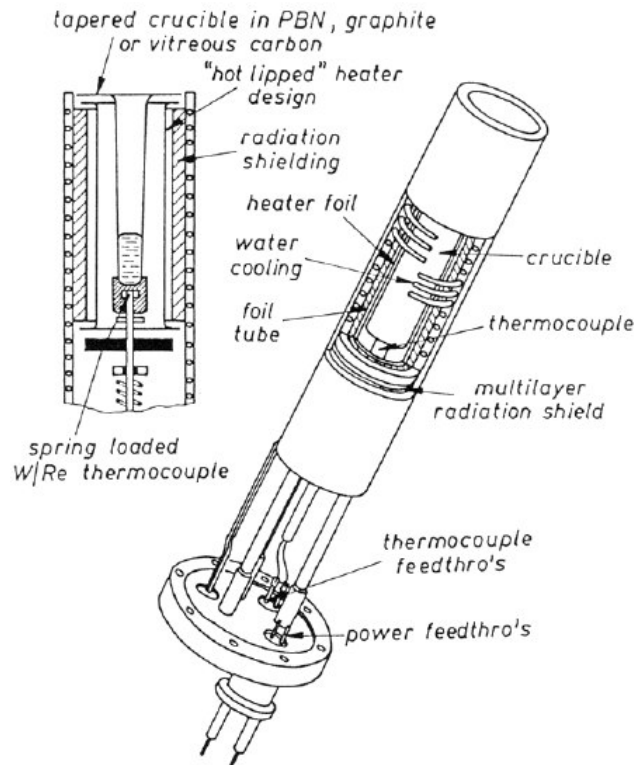


Figure III-23. Evaporation cell description [33].

Two MBE systems were used for our experiments. All the technical data described above apply to both systems. Here are the specific characteristics of each system:

- OPUS 45 from RIBER at the University of Illinois at Chicago (Microphysics Laboratory) contains 5 evaporation cells filled with: CdTe (2 cells), Te₂, Zn and As₄. The cells are water-cooled and the crucible can contain up to 50 cm³ of material. The chamber is designed to grow on radiatively heated substrates with a diameter up to 5 inches. The temperature of the substrate is read from a K-type thermocouple attached between the sample and the heater, as close to the sample as possible;
- Customized MBE from RIBER at the LPEM contains 3 evaporation cells: CdTe, Te₂ and As₄. The cells have a capacity of 25 and 35 cm³ depending on the cell. Because of the design of the heater and the sample holder transfer system, the loaded sample cannot be larger than 1 cm². The sample can be heated by radiation or by passing a current through the sample (this method is called direct heating in the following text). For radiative heating, the temperature is calibrated with a thermocouple welded on a Si sample radiatively heated and a 2.4 μm optical pyrometer is focused on the sample with an emissivity adjusted so that the read temperature matches the temperature measured with the thermocouple. For the direct heating mode, a calibration curve is drawn using the pyrometer with the same settings.

The OPUS 45 chamber is used to grow the layers of CdTe(211)B/ZnTe(211)B/As/Si(211) and to check the selective growth of CdTe on Si(100) pillars patterned on SiO₂ (see chapter V). The LPEM chamber is used to study the selective growth of CdTe on CdTe pillars patterned on Si(211) naturally oxidized.